CRYSTAL GROWTH & DESIGN

pubs.acs.org/crystal

Article

Spin-Crossover in a New Iron(II)/Di(pyrazolyl)pyridine Complex with a Terpyridine Embrace Lattice. Thermally Induced Excited Spin State Trapping and Clarification of a Structure−Function Correlation

Published as part of a Crystal Growth and Design virtual special issue on Molecular Magnets and Switchable Magnetic Materials

Evridiki Michaels, Izar Capel Berdiell, Hari Babu Vasili, Christopher M. Pask, Mark J. Howard, Oscar Cespedes, and Malcolm A. Halcrow*

Cite This: *Cryst. Growth Des.* 2022, 22, 6809−6817

Read Online

ACCESS | Metrics & More | Article Recommendations | Supporting Information

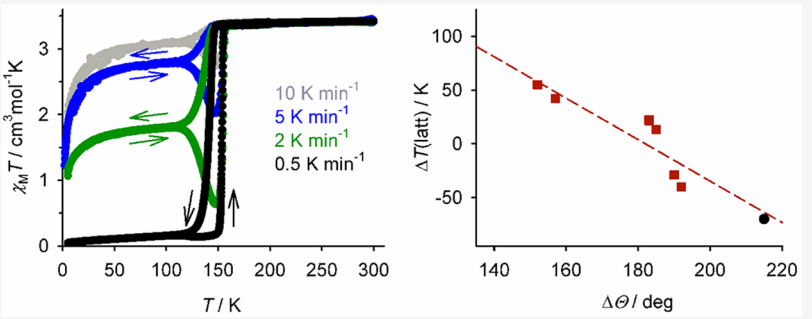

ABSTRACT: The complex salts $[FeL_2]X_2$ (**1X$_2$**; *L* = 2,6-di{4-fluoropyrazol-1-yl}pyridine; X^- = BF_4^- or ClO_4^-) exhibit abrupt spin-transitions with narrow thermal hysteresis, at $T_{1/2}$ = 164 K (X^- = BF_4^-) and 148 K (X^- = ClO_4^-). The transition in **1**$[ClO_4]_2$ is complicated by efficient thermally induced excited spin-state trapping (TIESST) of its high-spin state below ca. 120 K, and the fully low-spin state was achieved only inside the magnetometer at a scan rate of 0.5 K min^{-1}. Crystals of **1**$[BF_4]_2$ are tetragonal ($P\bar{4}2_1c$, *Z* = 2; phase 1) at 300 K but transform to a highly twinned monoclinic phase 2 ($P2_1$, *Z* = 2) at 285 ± 5 K. These are forms of the "terpyridine embrace" crystal lattice, which often affords cooperative spin-transitions in iron/di(pyrazolyl)pyridine complexes. Phase 2 of high-spin **1**$[BF_4]_2$ shows a significant temperature dependence by powder diffraction, which reflects increased canting of the monoclinic unit cell as the temperature is lowered. In contrast, **1**$[ClO_4]_2$ retains phase 2 between 100 and 300 K, and was crystallographically characterized in its thermally trapped metastable high-spin state at 100 K, as well as its thermodynamic high- and low-spin forms at higher temperatures. The spin-crossover transition temperature in **1**$[ClO_4]_2$ and related compounds correlates well with a parameter describing angular changes to the metal coordination sphere during the transition but not with other commonly used structural indices. The TIESST metastable high-spin state of **1**$[ClO_4]_2$ shows no single molecule magnet properties at 2 K.

INTRODUCTION

Spin-crossover (SCO) materials undergo a reversible high-to-low spin-state transition under the influence of a temperature change or another physical stimulus.[1−3] SCO transitions can be first or second order in the solid state[4,5] and induce changes in several useful materials properties.[2,6−10] That has led to development of prototype macro-, micro-, or nanoscale applications containing SCO materials as switching components.[11−15] The range of measurement techniques that can be applied to SCO transitions[3] also makes them valuable model systems, for atomistic studies of phase transitions and reaction dynamics in molecular crystals.[16,17]

Crystal engineering of SCO switching functionality is an important step toward widening their applicability. However, there are few generalizable structure−function relationships for SCO materials that have the necessary predictive value.[5,18,19] With that in mind, we investigated empirical correlations between the molecular structure and SCO transition temper-

Received: August 30, 2022
Revised: September 23, 2022
Published: September 28, 2022

https://doi.org/10.1021/acs.cgd.2c00980
Cryst. Growth Des. 2022, 22, 6809−6817

ature ($T_{1/2}$) in $[Fe(bpp^{R,Y})_2]X_2$ derivatives (Chart 1).[20] A library of >100 such compounds is now available, exhibiting a

Chart 1. Top: Structure of $[Fe(bpp^{R,Y})_2]X_2$[a] and Bottom: the New $bpp^{R,Y}$ Ligand *L* (R = H, Y = F)

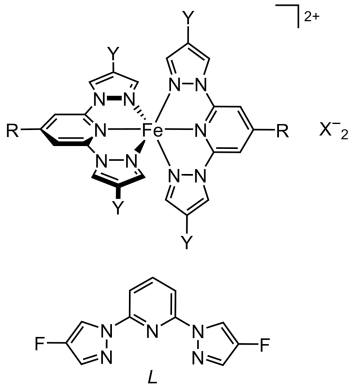

[a]X^- = a monovalent anion; the parent complex $[Fe(bpp)_2]^{2+}$ has R = Y = H).

range of spin-state behaviors.[21] Two separate factors influence $T_{1/2}$ in the solid state: the ligand field experienced by the individual iron switching centers and the physical constraints of the solid lattice in which those centers are embedded. The difference between $T_{1/2}$ in solution and in the solid state, ΔT(latt), was found to be a useful measure of the lattice contribution toward $T_{1/2}$.[20]

Groups of isomorphous $[Fe(bpp^{R,Y})_2]X_2$ compounds exhibit ΔT(latt) behaviors which are self-consistent within each group but different from each other. That is, different modes of crystal packing influence $T_{1/2}$ in different ways. The geometry of the complex's inner coordination sphere, and how this changes during SCO, appeared to be the most important structural influence on ΔT(latt).[20] One of the lattices investigated in that study is the terpyridine embrace.[22] This is often adopted by homoleptic complexes of 2,2′:6′,2″-terpyridine and related ligands, including $[Fe(bpp)_2][BF_4]_2$ and its derivatives with methyl or halogen ligand substituents (Chart 1).[23] The existence of a relationship between molecular geometry and ΔT(latt) was clearest for this structure type. However, its detailed origin could not be identified because the structural parameters examined tended to correlate with each other in the analysis.[20]

We now report a new $bpp^{R,Y}$ derivative, 2,6-di(4-fluoropyrazol-1-yl)pyridine (*L*), and its iron complex. The salts $[FeL_2]X_2$ (**1X$_2$**; X^- = BF_4^- or ClO_4^-) exhibit terpyridine embrace crystal packing and exhibit features which are new for this lattice type, including thermally induced excited spin-state trapping (TIESST) at low temperatures.[24] Comparison of **1X$_2$** with our previous ΔT(latt) analysis sheds new light on how $T_{1/2}$ is influenced by the molecular structure in terpyridine embrace crystals.

EXPERIMENTAL SECTION

Synthesis and characterization data for *L* are given in the Supporting Information. Unless otherwise stated, reagents and solvents were purchased commercially and used as supplied.

Caution. Although we have experienced no problems when using 1[ClO$_4$]$_2$, metal-organic perchlorates are potentially explosive and should be handled with care in small quantities.

Synthesis of [Fe*L*$_2$][BF$_4$]$_2$ (1[BF$_4$]$_2$). A mixture of *L* (0.20 g, 0.81 mmol) and $Fe[BF_4]_2{\cdot}6H_2O$ (0.14 g, 0.40 mmol) in nitromethane (10 cm^3) was stirred at room temperature until all of the solid had dissolved. The dark yellow solution was filtered, and the yellow polycrystalline complex was precipitated by slow addition of diethyl ether (50 cm^3). Elem anal. Found (calcd) for $C_{22}H_{14}B_2F_{12}FeN_{10}$ C 36.7 (36.5), H, 1.80 (1.95), N 19.1 (19.4) %. ^{1}H NMR (CD_3CN) δ −1.2 (2H, Py H^4), 54.4, 55.3 (both 4H, Py $H^{3/5}$ and Pz H^5), 65.4 (4H, Pz H^3).

Synthesis of [Fe*L*$_2$][ClO$_4$]$_2$ (1[ClO$_4$]$_2$). Method as for **1**[BF$_4$]$_2$, using $Fe[ClO_4]_2{\cdot}6H_2O$ (0.15 g, 0.40 mmol). The product was a yellow polycrystalline solid. Yield 51 mg, 72%. Elem anal. Found (calcd) for $C_{22}H_{14}Cl_2F_4FeN_{10}O_8$ C 35.3 (35.3), H, 1.87 (1.88), N 18.6 (18.7) %.

SINGLE CRYSTAL X-RAY STRUCTURE ANALYSES

Single crystals were obtained by slow diffusion of diethyl ether vapor into filtered solutions of the complexes in nitromethane. Crystals of phase 2 of **1**[BF$_4$]$_2$ were grown by this method inside a freezer at 255 K and were kept cold over dry ice during the mounting process. The other crystals were grown and handled under ambient conditions. Unless otherwise stated, the same crystal was used for data collections at multiple temperatures.

Diffraction data were collected with an Agilent Supernova dual source diffractometer using monochromated Cu-K_a radiation (λ = 1.54184 Å). Experimental details of each structure determination, and full details of all the crystallographic refinements, are given in the Supporting Information (Tables S1 and S2). The structures were solved by direct methods (*SHELXS*) and developed by full least-squares refinement on F^2 (*SHELXL-2018*).[25] Crystallographic figures were prepared using *X-SEED*,[26] and structural parameters tabulated in the Supporting Information were calculated with *Olex 2*.[27]

OTHER MEASUREMENTS

Elemental analyses were performed by the microanalytical services at the London Metropolitan University School of Human Sciences. Electrospray mass spectra were recorded on a Bruker MicroTOF-q instrument from $CHCl_3$ solution. Diamagnetic NMR spectra employed a Bruker AV3HD spectrometer operating at 400.1 (^{1}H), 100.6 (^{13}C) or 376.5 MHz (^{19}F). Paramagnetic ^{1}H NMR spectra were obtained with a Bruker AV3 spectrometer operating at 300.1 MHz. Powder diffraction data were recorded using a Bruker D8-A25 diffractometer in transmission capillary geometry, with a Ge(111) Johanssen monochromator and a Lynxeye detector, using Cu-$K_{\alpha 1}$ radiation (λ = 1.5406 Å). The diffractometer was fitted with an Oxford Cryostream low-temperature device.

Magnetic susceptibility measurements were performed using a Quantum Design MPMS-3 VSM magnetometer, in an applied field of 5000 G. Diamagnetic corrections for the samples were estimated from Pascal's constants;[28] a diamagnetic correction for the sample holder was also applied to the data. Susceptibility measurements in solution were obtained by the Evans method using a Bruker AV-NEO spectrometer operating at 500.2 MHz.[29] A diamagnetic correction for the sample,[28] and a correction for the variation of the density of the CD_3CN solvent with temperature,[30] were

https://doi.org/10.1021/acs.cgd.2c00980
Cryst. Growth Des. 2022, 22, 6809−6817

applied to these data. Thermodynamic parameters and the equilibrium midpoint temperature ($T_{1/2}$) were derived by fitting these data to eqs 1 and 2, where nHS(T) is the high-spin fraction of the sample at temperature T:

$$\ln\{[1 - n\mathrm{HS}(T)]/n\mathrm{HS}(T)\} = \Delta H/RT - \Delta S/R \quad (1)$$

$$\Delta S = \Delta H/T_{1/2} \quad (2)$$

RESULTS AND DISCUSSION

The ligands bpp^{H,Cl}, bpp^{H,Br}, and bpp^{H,I} were originally prepared by electrophilic halogenation of preformed, unsubstituted bpp (Chart 1).[31−33] However, they can be synthesized more simply from 2,6-difluoropyridine and the appropriate 4-halo-1*H*-pyrazole, which are all commercially available.[34] Thus, the new ligand *L* was obtained in 81% yield by the reaction of 2,6-difluoropyridine with 2 equiv of 4-fluoropyrazole in *N*,*N*-dimethylformamide, in the presence of NaH as the base. Treatment of *L* with 0.5 equiv of $Fe[BF_4]_2{\cdot}6H_2O$ or $Fe[ClO_4]_2{\cdot}6H_2O$ in nitromethane afforded $[FeL_2]X_2$ (**1X$_2$**; X^- = BF_4^- or ClO_4^-). The complex salts readily afford well-formed yellow prisms from common organic solvents, using diethyl ether as the antisolvent. However, while these crystals did not contain lattice solvent, their diffraction quality was dependent on the crystallization solvent used. The crystallographic measurements described below employed crystals grown from nitromethane/diethyl ether, which were found to give the best results.

Both materials are high-spin at room temperature but exhibit abrupt, hysteretic spin-transitions on cooling. **1**$[BF_4]_2$ exhibits a complete SCO with $T_{1/2}\downarrow$ = 156 and $T_{1/2}\uparrow$ = 172 K at a scan rate of 5 K min^{-1}, that is, a thermal hysteresis ($\Delta T_{1/2}$) of 16 K. The transition for **1**$[ClO_4]_2$ lies at a slightly lower temperature and proceeds only to ca. 25% completeness on cooling at a 5 K min^{-1} scan rate. Rewarming the sample led to a pronounced decrease in $\chi_M T$ above 110 K, followed by an abrupt increase at 150 K where the sample reverted to its high-spin form. That χ_MT vs T profile is characteristic of thermally induced excited spin state trapping (TIESST) of the high-spin state at low temperatures.[24,35−41] This arises when the spin-transition is kinetically slow on the time scale of the measurement, which can occur for transitions occurring below ca. 100 K. The sample, or a fraction of it, remains trapped in a metastable high-spin state if the sample is cooled too rapidly. Thermal relaxation to its thermodynamic low-spin form occurs only when sample is rewarmed, producing enough thermal lattice energy to overcome the kinetic barrier to SCO. TIESST has been observed in a number of $[Fe(bpp)_2]X_2$ derivatives whose spin-transitions lie within that temperature range.[42−46]

The kinetic origin of these effects was confirmed by repeating the measurement at different scan rates. At 10 K min^{-1}, 90% of the sample remained high-spin, showing almost complete thermal trapping of the high-spin state. Conversely, scanning at 0.5 K min^{-1} revealed the full transition profile, with <5% of the sample remaining high-spin below 100 K. Under those conditions, **1**$[ClO_4]_2$ exhibits $T_{1/2}\downarrow$ = 141, $T_{1/2}\uparrow$ = 154 and $\Delta T_{1/2}$ = 13 K.

Crystals of **1**$[BF_4]_2$ were characterized at 300 K in the tetragonal space group $P\bar{4}2_1c$, with Z = 2 (phase 1). The high-spin cation lies on a site of crystallographic $\bar{4}$ symmetry, with one-quarter of a complex cation and half a disordered BF_4^- anion in its asymmetric unit (Figure 2, Table 1). Unexpectedly, however, the crystal became twinned when cooled to 280 K.

Table 1. Selected Metric Parameters and Structural Indices for Phase 1 of 1$[BF_4]_2$[a]

Fe−N{pyridyl}/Å	2.132(6)	V_{Oh}/Å^3	12.56(2)
Fe−N{pyrazolyl}/Å	2.204(5)	Σ/deg	161.2(4)
		Θ/deg	529
		ϕ/deg	180
		θ/deg	90

[a]The complex molecule in this phase has crystallographically imposed $\bar{4}$ symmetry. V_{Oh} is the volume defined by the FeN_6 coordination octahedron.[18] Σ measures the deviation of a metal ion from an ideal octahedral geometry, while Θ indicates its distortion toward a trigonal prismatic structure.[18,50] ϕ is the *trans*-N{pyridyl}-Fe-N{pyridyl} bond angle, while θ is the dihedral angle between the least-squares planes of the two tridentate ligands.[47] More detailed definitions and discussion of these parameters are in the Supporting Information.

This was explained by the powder diffraction data described below, showing the material undergoes a crystallographic phase change at 285 ± 5 K. Low-temperature phase 2 (monoclinic, $P2_1$, Z = 2) is isomorphous with $[Fe(bpp)_2][BF_4]_2$[47] and some other $[Fe(bpp^{H,Y})_2]X_2$ derivatives (Chart 1).[23,48] Unfortunately, phase 2 consistently exhibited rotational twinning, even in crystals grown below the phase transition temperature at 255 K. As a result, only preliminary structure solutions of phase 2 of **1**$[BF_4]_2$ were achieved (Figure S3).[49]

Crystals of **1**$[ClO_4]_2$ are isomorphous with phase 2 of **1**$[BF_4]_2$ at room temperature and retain that symmetry between 300 and 100 K. These crystals were more tractable, and full structure refinements were achieved at four temperatures. Analyses at 250, 180, and 100 K each revealed a fully high-spin complex, showing the crystal had undergone complete TIESST trapping of its high-spin state when cooled to 100 K on the diffractometer (Table 2). The low-spin crystal was then achieved by slowly rewarming it to 145 K, which allowed it to relax to its thermodynamic low-spin form at that temperature (Figure 1).

Phase 1 and 2 are both forms of the terpyridine embrace packing motif, with cations packed into interdigitated layers by translation in the *ab* plane (Figure S6).[22] The cations in phase 1 have crystallographic $\bar{4}$ symmetry, with the unique symmetry axes of each cation being coparallel with the unit cell *c* axis. In contrast, in phase 2 the cations have no internal symmetry, and molecules in adjacent cation layers are no longer strictly coparallel. Rows of cations in each layer are horizontally offset by up to 0.8 Å along *c*, causing a canting of the layers, which is reflected in the unit cell β angle (Figure 2). Nearest neighbor molecules in the layers interact predominantly through edge-to-face C−F···π contacts (Figures S7−S9 and Table S5). These induce a bowed conformation at ligand N(20)−F(37), which is especially pronounced in the high-spin form of phase 2 (Figure S8). Face-to-face π···π interactions within the layers are longer and weak, reflecting the steric influence of the F substituents.

These structural changes were monitored by variable temperature X-ray powder diffraction. The data clearly show the phase 1 → 2 transformation in **1**$[BF_4]_2$ between 290 and 280 K, and indicate that the powder pattern of phase 2 evolves continuously on cooling between 280 and 140 K (Figure 3). Further cooling to 120 K leads to simplification of the powder pattern, showing the material has transformed to its low-spin state. Simulations derived from phase 1 and the preliminary crystal structure solutions of phase 2 are an excellent match for these data (Figure S10).

https://doi.org/10.1021/acs.cgd.2c00980
Cryst. Growth Des. 2022, 22, 6809−6817

Table 2. Selected Metric Parameters and Structural Indices for $1[ClO_4]_2$ at Different Temperatures[a]

T/K (spin state)	250 (high-spin)	180 (high-spin)	100 (high-spin, thermally trapped)	145 (low-spin)
Fe−N{pyridyl}/Å	2.139(4), 2.145(5)	2.134(3), 2.141(3)	2.137(3), 2.141(3)	1.899(8), 1.906(7)
Fe−N{pyrazolyl}/Å	2.179(7)−2.202(6)	2.184(4)−2.195(4)	2.179(4)−2.196(4)	1.983(8)−1.998(8)
V_{Oh}/Å^3	12.46(2)	12.436(14)	12.427(12)	9.74(3)
Σ/deg	156.9(7)	155.7(5)	157.4(4)	89.5(11)
Θ/deg	515	509	509	294
ϕ/deg	177.7(2)	178.28(13)	178.19(13)	178.2(3)
θ/deg	88.46(6)	88.07(4)	87.94(3)	88.49(8)

[a]See Table 1 or the Supporting Information for a description of the bond length and angle parameters in the table.

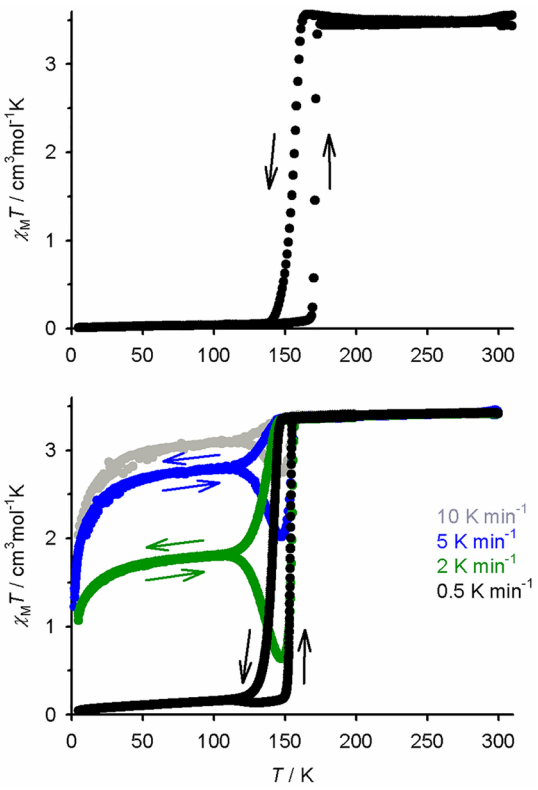

Figure 1. Magnetic susceptibility data for $1[BF_4]_2$ (top) and $1[ClO_4]_2$ (bottom), at different thermal scan rates.

SCO in the powder diffractometer occurred at a slightly lower temperature than expected from the magnetic measurement (Figure 1). That could reflect the different conditions of the two measurements[51] or simply the accuracy of the temperature control on the powder diffractometer at such low temperatures, which are near the limit of the cryostat.

Powder diffraction data for $1[ClO_4]_2$ confirm it is isomorphous with phase 2 of $1[BF_4]_2$ at 290 K but show some differences compared to the BF_4^- salt (Figure S11). The data from $1[ClO_4]_2$ at room temperature resemble $1[BF_4]_2$ at 190 K, and the evolution of the high-spin powder pattern of $1[ClO_4]_2$ on cooling to $T_{1/2}$ is also less pronounced. In addition, the powder pattern of $1[ClO_4]_2$ at 120 K is a mixture of the low-spin and high-spin phases, in an approximately 2:1 ratio (Figure S12). That implies SCO occurred incompletely on cooling the sample, so ca. one-third of its iron centers remained thermally trapped in its high-spin state at 120 K, as before. A powder pattern of the pure low-spin phase of $1[ClO_4]_2$ was not achieved.

The temperature-dependence of the diffraction data from high-spin phase 2 of $1[BF_4]_2$ cannot be explained in detail (Figure 3). However, single crystal unit cell parameters show its unit cell β angle increases significantly on cooling, from 91.525(14)° at 280 K to 94.782(10)° at 220 K (Table S1), which is confirmed by the powder diffraction simulations (Figure S10). That should reflect the translation of rows of complex molecules along c as the temperature is lowered, so the terpyridine embrace layers become increasingly canted as β gets larger (Figure 2). Such canting of the lattice could be accompanied by distortions of the molecular structure,[52] although that is unclear without full structure refinements. In contrast, β for high-spin $1[ClO_4]_2$ shows less variation over a wider temperature range, from 95.863(5)° at 250 K to 96.589(2)° at 100 K.

A handful of iron(II) SCO materials are single-molecule magnets (SMMs)[53] in their kinetically trapped high-spin state, generated photochemically at low temperature in the light-induced excited spin state trapping (LIESST) experiment.[54−56] Such materials can exist in their low-spin form, or in two spin orientations of their high-spin state, making them magnetically tristable. With that in mind, the TIESST high-spin form of $1[ClO_4]_2$ was screened for SMM properties with AC magnetic susceptibility measurements. However, no out-of-phase magnetic moment was observed at temperatures ≥2 K, in an applied field or in zero-field. Hence high-spin $1[ClO_4]_2$ is not an SMM under these conditions (Figure S13).[57]

Magnetic data from $1[BF_4]_2$ in CD_3CN show that the complex is fully high-spin in solution at room temperature. Cooling to 238 K (just above the freezing point of the solution) results in a small decrease in $\chi_M T$, which is consistent with the onset of a typically gradual SCO equilibrium (Figure S14). Fitting the data to a thermodynamic equilibrium [eqs 1 and 2] yielded $T_{1/2}$ = 218(4) K, ΔH = −22(2) kJ mol^{-1}, and ΔS = 101(9) J mol^{-1} K^{-1}. Measurement at a lower temperature to yield more accurate fitting parameters was not possible because of the complex's low solubility in suitable solvents like $\{CD_3\}_2CO$. Nonetheless, the thermodynamic parameters from the analysis are typical for $[Fe(bpp)_2]X_2$ derivatives in solution.[58] The $T_{1/2}$ value is also consistent with previous data from the chloro-, bromo-, and iodo-substituted analogues of $1[BF_4]_2$, based on the electronegativities of the respective halo substituents (Figure S15).[58]

STRUCTURE: FUNCTION CORRELATIONS

As described above, we have proposed ΔT(latt) as a way to separate contributions from the individual molecular ligand field, and the extended solid lattice, to the SCO temperature in solid materials [eq 3].[20]

$$\Delta T(\text{latt}) = T_{1/2}(\text{solid}) - T_{1/2}(\text{solution}) \quad (3)$$

A positive ΔT(latt) shows the lattice stabilizes the low-spin form of a material, leading to a higher temperature SCO than

https://doi.org/10.1021/acs.cgd.2c00980
Cryst. Growth Des. 2022, 22, 6809−6817

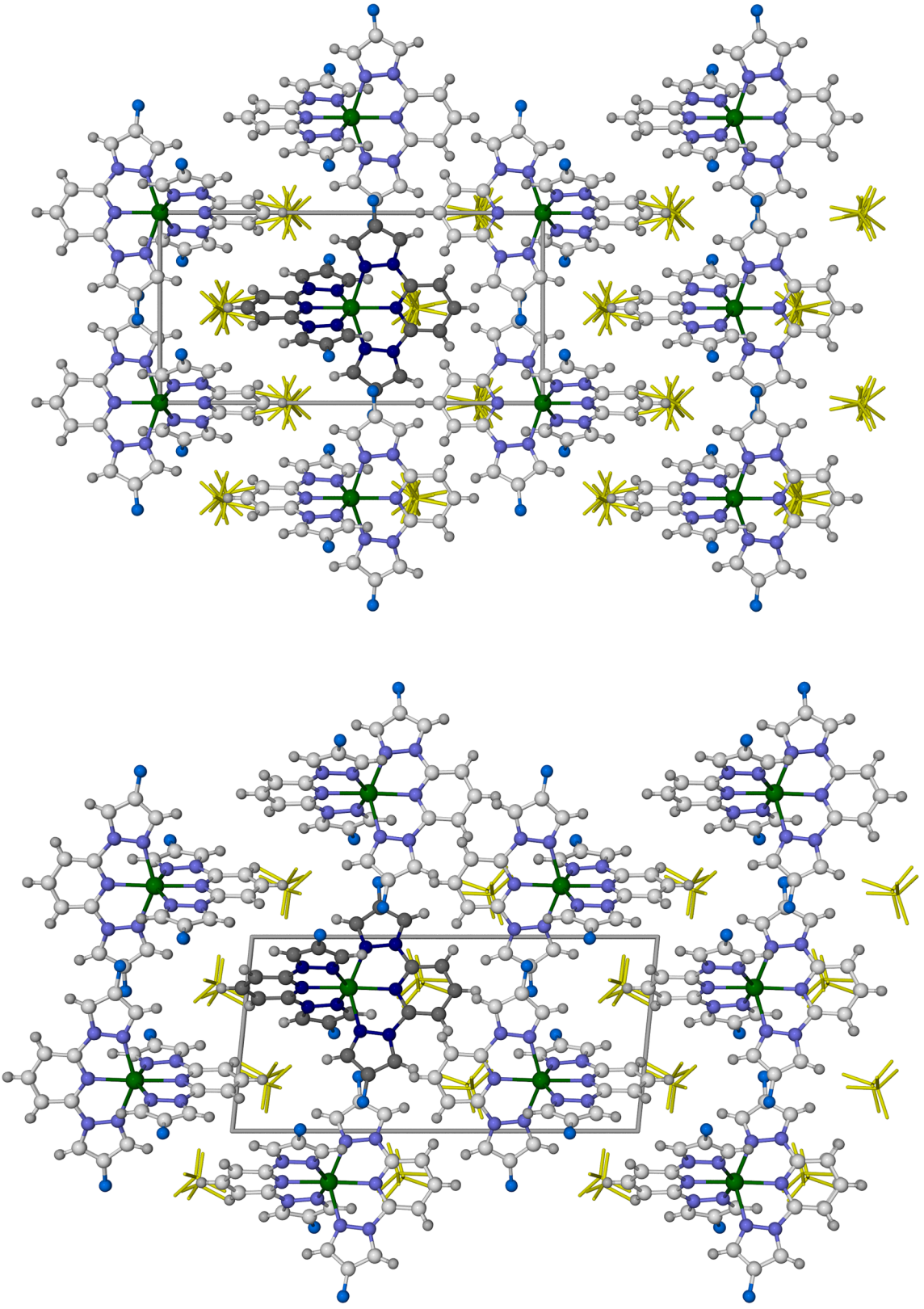

Figure 2. Packing diagrams for phase 1 of $\mathbf{1}[\mathbf{BF_4}]_2$ (top) and phase 2 of $\mathbf{1}[\mathbf{ClO_4}]_2$ at 250 K (bottom). Both views are parallel to the [010] crystal vector, with the *c* axis horizontal. One cation is highlighted with dark coloration, and the anions are de-emphasized for clarity. Color code: C, white or dark gray; H, pale gray; Fe, green; N, pale or dark blue; BF_4^- or ClO_4^-, yellow.

for the same compound in solution, and *vice versa*. A survey of $[Fe(bpp^{R,Y})_2]X_2$ derivatives with the terpyridine embrace packing motif showed that lattice type supports both positive and negative ΔT(latt) values and that ΔT(latt) for those compounds correlates reasonably with many of the molecular structure indices listed in Tables 1 and 2. The latter fact made

https://doi.org/10.1021/acs.cgd.2c00980
Cryst. Growth Des. 2022, 22, 6809−6817

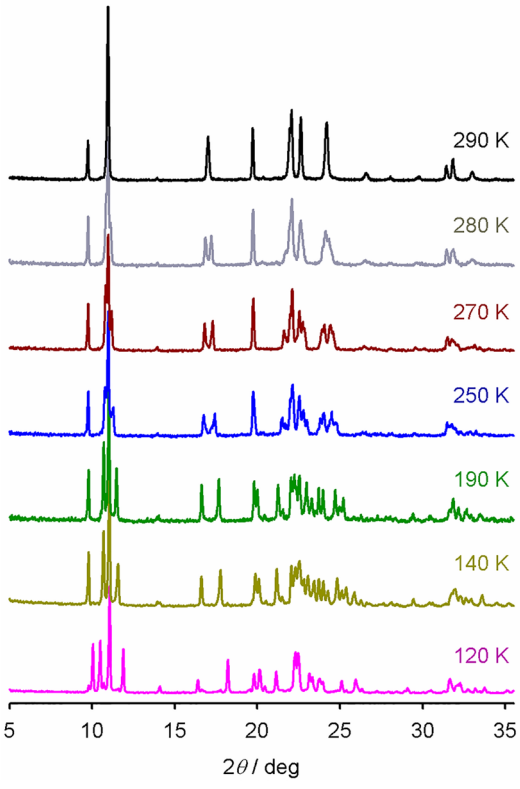

Figure 3. Variable temperature X-ray powder diffraction data for $\mathbf{1}[BF_4]_2$. Crystallographic simulations of some of these data are shown in Figure S10.

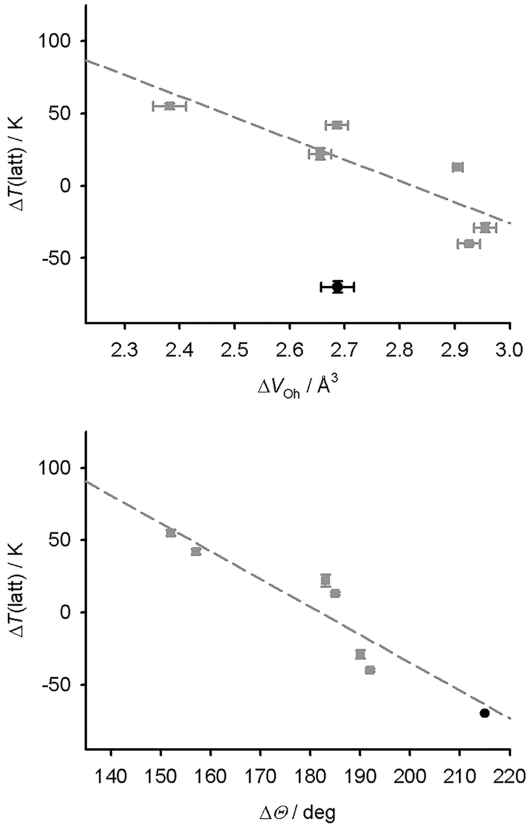

Figure 4. Plots of ΔT(latt) vs ΔV_{Oh} (top) and $\Delta\Theta$ (bottom) for $[Fe(bpp^{R,Y})_2]X_2$ derivatives in a terpyridine embrace lattice. The gray data points and lines show the structure−function correlations from ref 20, while data from $\mathbf{1}[ClO_4]_2$ are shown in black.

it impossible to firmly identify which aspect of their structural chemistry had the greatest influence on ΔT(latt).

ΔT(latt) for $\mathbf{1}[BF_4]_2$ and $\mathbf{1}[ClO_4]_2$ is −54 and −70 K respectively, showing the terpyridine embrace lattice greatly stabilizes the high-spin state of those compounds. Other $[Fe(bpp^{R,Y})_2]X_2$ derivatives with terpyridine embrace crystal packing show $-49 \leq \Delta T(\text{latt}) \leq +55$ K (Table S6).[20] Figure 4 shows two correlations from ref 20, plotting ΔT(latt) against indices measuring changes in the Fe−N bond lengths (ΔV_{Oh}) and N−Fe−N angles ($\Delta\Theta$) during SCO.[49] The published ΔV_{Oh} vs ΔT(latt) correlation overestimates ΔT(latt) (and thus $T_{1/2}$) for $\mathbf{1}[ClO_4]_2$, by ca. 100 K. The only parameter from our previous analysis that predicts ΔT(latt) for $\mathbf{1}[ClO_4]_2$ is $\Delta\Theta$ (Figure 4, bottom),[18,50] that is, the change in the angular structure between the spin states within the $[FeN_6]$ core, along the O_h/D_{3h} distortion pathway.[21]

Hence, the angular change in the inner metal coordination sphere appears to form the main lattice contribution to $T_{1/2}$, for $[Fe(bpp^{R,Y})_2]X_2$ derivatives in a terpyridine embrace crystal. Specifically, a greater angular change stabilizes the high-spin state of the complex and lowers $T_{1/2}$ to a predictable extent. That is intuitively reasonable, since the high-spin state of $[Fe(bpp^{R,Y})_2]^{2+}$ complexes is structurally plastic and easily deformed, while their more rigid low-spin state strongly prefers a regular octahedral coordination geometry.[59] A lattice that imposes a more distorted coordination geometry on a complex will destabilize its low-spin state, thus making ΔT(latt) more negative and lowering $T_{1/2}$.

The $\Delta\Theta = 215°$ distortion change during SCO in $\mathbf{1}[ClO_4]_2$ is among the highest for any $[Fe(bpp^{R,Y})_2]X_2$ derivative. While Θ for low-spin $\mathbf{1}[ClO_4]_2$ lies within the usual range, its high-spin Θ value is unusually large (Table 2); other SCO-active $[Fe(bpp^{R,Y})_2]X_2$ complexes exhibit $\Theta < 500°$ in their high-spin forms.[5,20] Since Θ is a torsion angle parameter, it cannot be simply related to the bond lengths and angles at Fe(1) (Chart S1). However, ligand N(20)−F(37) in the high-spin complex shows a pronounced bow-shaped conformation, induced by intermolecular C−F···π contacts (Figure S8). This displaces the pyrazolyl donor atoms N(27) and N(33) out of their meridional plane, increasing the distortion of Fe(1) along the O_h/D_{3h} pathway and affording a larger value of Θ.[21]

CONCLUSION

We noted 15 years ago that $[Fe(bpp)_2]X_2$ derivatives crystallizing in a terpyridine embrace lattice often exhibit very consistent spin-transitions, which occur abruptly with a small thermal hysteresis of 2−3 K.[23] Few new examples of that family of materials have been published since our initial observation,[58,60] but $\mathbf{1}[BF_4]_2$ and $\mathbf{1}[ClO_4]_2$ now confirm that trend. While SCO thermal hysteresis can be scan-rate dependent,[51] the 13 K hysteresis shown by $\mathbf{1}[ClO_4]_2$ at the slow scan rate of 0.5 K min^{-1} is unusually wide for a material with this structure type.

SCO cooperativity depends largely on changes to the strength, geometry, and anisotropy of intermolecular contacts in the crystal during SCO. The large $\Delta\Theta$ distortion in $\mathbf{1}[ClO_4]_2$ is a property of its inner coordination sphere, which should not influence its thermal hysteresis unless it reflects a larger structure change in the molecule as a whole.[20] Hysteretic spin-transitions in $[Fe(bpp^{R,Y})_2]X_2$ derivatives can be asso-

https://doi.org/10.1021/acs.cgd.2c00980
Cryst. Growth Des. 2022, 22, 6809−6817

ciated with a rearrangement of the ligands about the metal ion during SCO, which manifests in their *trans*-N{pyridyl}−Fe−N{pyridyl} angle (ϕ; Tables 1 and 2).[44,61−63] However, the change in ϕ between the spin states of $\mathbf{1}[\mathbf{ClO_4}]_2$, $\Delta\phi$ = −0.55(9)°, is too small to be significant (Table S7). Rather, the SCO hysteresis shown by $\mathbf{1}[\mathbf{BF_4}]_2$ and $\mathbf{1}[\mathbf{ClO_4}]_2$ may reflect the steric influence of their fluoro substituents on their crystal packing, which leads to a significant conformational distortion of one *L* ligand (Figures S8−S9). A wider survey of the SCO cooperativity in $[Fe(bpp^{R,Y})_2]X_2$ complexes with terpyridine embrace packing is in progress and will be reported separately.

SCO in $[Fe(bpp^{R,Y})_2]X_2$ derivatives that extends toward 100 K is often incomplete, with a residual high-spin fraction of the sample being trapped in its high-spin form below that temperature.[42−46] However, the TIESST effect shown by $\mathbf{1}[\mathbf{ClO_4}]_2$ is notably efficient, on the diffractometer and in the SQUID magnetometer.[35−41] The high-spin and low-spin forms of $\mathbf{1}[\mathbf{ClO_4}]_2$ can be produced selectively below 100 K, by cooling at >10 K min^{-1} or <0.5 K min^{-1} respectively (Figure 1). While $\mathbf{1}[\mathbf{ClO_4}]_2$ itself is not an SMM,[57] bistable multifunctional materials could still be produced from the $\mathbf{1}[\mathbf{ClO_4}]_2$ host lattice containing functional dopant molecules.[64,65]

Phase 2 of $\mathbf{1}[\mathbf{BF_4}]_2$ shows a significant temperature dependence in its high-spin state (Figure 3). That reflects an increase of the monoclinic unit cell β angle at lower temperatures, which should reflect a gradual canting of the terpyridine embrace cation layers as the sample is cooled (Figure 2). Unfortunately, more detailed investigation of this temperature dependence was prevented by the persistent twinning of phase 2.[49] High-spin $\mathbf{1}[\mathbf{ClO_4}]_2$ is isomorphous with phase 2, however, with a more canted unit cell at room temperature, which shows a much smaller temperature dependence.

Our previous work demonstrated that ΔT(latt) for $[Fe(bpp^{R,Y})_2]X_2$ derivatives in a terpyridine embrace lattice correlated with ΔV_{Oh}, $\Delta\Theta$, and with other measures of the structural changes occurring during SCO. That made it impossible to identify the detailed origin of the structure−function relationship. Comparing these published structure−function correlations with $\mathbf{1}[\mathbf{ClO_4}]_2$ confirms that only the $\Delta\Theta$ parameter reliably predicts ΔT(latt) in this system (Figure 4). That is, the lattice contribution to $T_{1/2}$(solid) arises mostly from the change in the angular coordination geometry at the iron center.

Gratifyingly, that agrees with an earlier conclusion from Guionneau et al. that $T_{1/2}$(solid) in a series of solid $[Fe(NCS)_2(NN)_2]$ (NN = a bidentate N-donor ligand) complexes shows a similar relationship with $\Delta\Theta$.[66] Importantly, most of the materials studied by Guionneau et al. also adopt different versions of the same crystal packing motif. Chemically, they mostly differ only in the identity of a peripheral aromatic Schiff base ligand substituent, so their $T_{1/2}$(solution) values should also be similar. That is, $T_{1/2}$(solid) ∝ ΔT(latt) for those compounds [eq 3]. This is a rare example where the same SCO structure−function relationship has been demonstrated for two different classes of material. Further experimental and computational studies will confirm how widely the observation can be generalized within SCO materials chemistry.

■ ASSOCIATED CONTENT

Data Availability Statement

Experimental data sets associated with this paper are available from the University of Leeds library (10.5518/1229).

Supporting Information

The Supporting Information is available free of charge at https://pubs.acs.org/doi/10.1021/acs.cgd.2c00980.

Synthetic details and characterization data for the new ligand *L*; experimental data, refinement procedures, and tabulated metric parameters for the crystal structure determinations; measured and simulated X-ray powder diffraction data; solution magnetic susceptibility measurements; and data for the structure−function correlation plots in Figure 4 (PDF)

Accession Codes

CCDC 2193311−2193315 contain the supplementary crystallographic data for this paper. These data can be obtained free of charge via www.ccdc.cam.ac.uk/data_request/cif, or by emailing data_request@ccdc.cam.ac.uk, or by contacting The Cambridge Crystallographic Data Centre, 12 Union Road, Cambridge CB2 1EZ, UK; fax: +44 1223 336033.

■ AUTHOR INFORMATION

Corresponding Author

Malcolm A. Halcrow − *School of Chemistry, University of Leeds, Leeds LS2 9JT, U.K.*; orcid.org/0000-0001-7491-9034; Email: m.a.halcrow@leeds.ac.uk

Authors

Evridiki Michaels − *School of Chemistry, University of Leeds, Leeds LS2 9JT, U.K.*

Izar Capel Berdiell − *Center for Material Science and Nanomaterials (SMN), University of Oslo, 0371 Oslo, Norway*

Hari Babu Vasili − *School of Physics and Astronomy, University of Leeds, Leeds LS2 9JT, U.K.*

Christopher M. Pask − *School of Chemistry, University of Leeds, Leeds LS2 9JT, U.K.*

Mark J. Howard − *School of Chemistry, University of Leeds, Leeds LS2 9JT, U.K.*

Oscar Cespedes − *School of Physics and Astronomy, University of Leeds, Leeds LS2 9JT, U.K.*; orcid.org/0000-0002-5249-9523

Complete contact information is available at: https://pubs.acs.org/10.1021/acs.cgd.2c00980

Notes

The authors declare no competing financial interest.

■ ACKNOWLEDGMENTS

This work was funded by the University of Leeds. The powder diffraction facility is supported by the Norwegian National Infrastructure for X-ray Diffraction and Scattering (RECX) and by the Research Council of Norway via the TomoCAT Researcher Project (No. 301619).

■ REFERENCES

(1) Gütlich, P., Goodwin, H. A., Eds. *Spin Crossover in Transition Metal Compounds I−III, Topics in Current Chemistry*; Springer-Verlag: Berlin, 2004; Vols. 233−235.

(2) Halcrow, M. A., Ed. *Spin-Crossover Materials - Properties and Applications*; John Wiley & Sons, Ltd.: New York, 2013; p 568.

(3) Zarembowitch, J.; Varret, F.; Hauser, A.; Real, J. A.; Boukheddaden, K. Spin Crossover Phenomenon − Preface and Introduction. *C. R. Chimie* **2018**, *21*, 1056−1059.
(4) Gütlich, P.; Hauser, A.; Spiering, H. Thermal and Optical Switching of Iron(II) Complexes. *Angew. Chem. Int. Ed* **1994**, *33*, 2024−2054.
(5) Halcrow, M. A. Structure:Function Relationships in Molecular Spin-Crossover Complexes. *Chem. Soc. Rev.* **2011**, *40*, 4119−4142.
(6) Kahn, O.; Kröber, J.; Jay, C. Spin Transition Molecular Materials for Displays and Data Recording. *Adv. Mater.* **1992**, *4*, 718−728.
(7) Gaspar, A. B.; Seredyuk, M. Spin Crossover in Soft Matter. *Coord. Chem. Rev.* **2014**, *268*, 41−58.
(8) Manrique-Juárez, M. A.; Rat, S.; Salmon, L.; Molnár, G.; Quintero, C. M.; Nicu, L.; Shepherd, H. J.; Bousseksou, A. Switchable Molecule-Based Materials for Micro- and Nanoscale Actuating Applications: Achievements and Prospects. *Coord. Chem. Rev.* **2016**, *308*, 395−408.
(9) Meng, Y.-S.; Liu, T. Manipulating Spin Transition to Achieve Switchable Multifunctions. *Acc. Chem. Res.* **2019**, *52*, 1369−1379.
(10) Wang, M.; Li, Z.-Y.; Ishikawa, R.; Yamashita, M. Spin Crossover and Valence Tautomerism Conductors. *Coord. Chem. Rev.* **2021**, *435*, 213819.
(11) Molnár, G.; Rat, S.; Salmon, L.; Nicolazzi, W.; Bousseksou, A. Spin Crossover Nanomaterials: From Fundamental Concepts to Devices. *Adv. Mater.* **2018**, *30*, 1703862.
(12) Reis, M. S. Magnetocaloric and Barocaloric Effects of Metal Complexes for Solid State Cooling: Review, Trends and Perspectives. *Coord. Chem. Rev.* **2020**, *417*, 213357.
(13) Enriquez-Cabrera, A.; Rapakousiou, A.; Piedrahita Bello, M.; Molnár, G.; Salmon, L.; Bousseksou, A. Spin Crossover Polymer Composites, Polymers and Related Soft Materials. *Coord. Chem. Rev.* **2020**, *419*, 213396.
(14) Coronado, E. Molecular Magnetism: from Chemical Design to Spin Control in Molecules, Materials and Devices. *Nature Rev. Mater.* **2020**, *5*, 87−104.
(15) Kipgen, L.; Bernien, M.; Tuczek, F.; Kuch, W. Spin-Crossover Molecules on Surfaces: From Isolated Molecules to Ultrathin Films. *Adv. Mater.* **2021**, *33*, 2008141. See DOI: 10.1002/adma.202105663 for the correction.
(16) Chergui, M.; Collet, E. Photoinduced Structural Dynamics of Molecular Systems Mapped by Time-Resolved X-ray Methods. *Chem. Rev.* **2017**, *117*, 11025−11065.
(17) Gaffney, K. J. Capturing Photochemical and Photophysical Transformations In Iron Complexes with Ultrafast X-Ray Spectroscopy and Scattering. *Chem. Sci.* **2021**, *12*, 8010−8025.
(18) Guionneau, P.; Marchivie, M.; Bravic, G.; Létard, J.-F.; Chasseau, D. Structural Aspects of Spin Crossover. Example of the $[Fe^{II}L_n(NCS)_2]$ Complexes. *Top. Curr. Chem.* **2004**, *234*, 97−128.
(19) Guionneau, P.; Marchivie, M.; Chastanet, G. Multiscale Approach of Spin Crossover Materials: a Concept Mixing Russian Dolls and Domino Effects. *Chem. − Eur. J.* **2021**, *27*, 1483−1486.
(20) Halcrow, M. A.; Capel Berdiell, I.; Pask, C. M.; Kulmaczewski, R. The Relationship Between Molecular Structure and Switching Temperature in a Library of Spin-Crossover Molecular Materials. *Inorg. Chem.* **2019**, *58*, 9811−9821.
(21) Kershaw Cook, L. J.; Mohammed, R.; Sherborne, G.; Roberts, T. D.; Alvarez, S.; Halcrow, M. A. Spin State Behaviour of Iron(II)/Dipyrazolylpyridine Complexes. New Insights from Crystallographic and Solution Measurements. *Coord. Chem. Rev.* **2015**, *289*−*290*, 2−12.
(22) Dance, I.; Scudder, M. Molecules Embracing in Crystals. *CrystEngComm* **2009**, *11*, 2233−2247.
(23) Pritchard, R.; Kilner, C. A.; Halcrow, M. A. Iron(II) Complexes with a Terpyridine Embrace Packing Motif Show Remarkably Consistent Cooperative Spin-Transitions. *Chem. Commun.* **2007**, *2007*, 577−579.
(24) Marchivie, M.; Guionneau, P.; Létard, J.-F.; Chasseau, D.; Howard, J. A. K. Thermal Trapped Iron(II) High Spin State Investigated by X-Ray Diffraction. *J. Phys. Chem. Solids* **2004**, *65*, 17−23.
(25) Sheldrick, G. M. Crystal Structure Refinement with *SHELXL*. *Acta Cryst. Sect. C: Struct. Chem.* **2015**, *71*, 3−8.
(26) Barbour, L. J. *X-Seed 4*: Updates to a Program for Small-Molecule Supramolecular Crystallography. *J. Appl. Crystallogr.* **2020**, *53*, 1141−1146.
(27) Dolomanov, O. V.; Bourhis, L. J.; Gildea, R. J.; Howard, J. A. K.; Puschmann, H. *OLEX2*: a Complete Structure Solution, Refinement and Analysis Program. *J. Appl. Crystallogr.* **2009**, *42*, 339−341.
(28) O'Connor, C. J. Magnetochemistry − Advances in Theory and Experimentation. *Prog. Inorg. Chem.* **1982**, *29*, 203−283.
(29) Schubert, E. M. Utilizing the Evans Method with a Superconducting NMR Spectrometer in the Undergraduate Laboratory. *J. Chem. Educ.* **1992**, *69*, 62.
(30) García, B.; Ortega, J. C. Excess Viscosity η^E, Excess Volume V^E, and Excess Free Energy of Activation ΔG^{*E} at 283, 293, 303, 313, and 323 K for Mixtures of Acetonitrile and Alkyl Benzoates. *J. Chem. Eng. Data* **1988**, *33*, 200−204.
(31) Zoppellaro, G.; Baumgarten, M. One-Step Synthesis of Symmetrically Substituted 2,6-Bis(pyrazol-1-yl)pyridine Systems. *Eur. J. Org. Chem.* **2005**, *2005*, 2888−2892. See DOI: 10.1002/ejoc.200500620 for the correction.
(32) Pritchard, R.; Lazar, H.; Barrett, S. A.; Kilner, C. A.; Asthana, S.; Carbonera, C.; Létard, J.-F.; Halcrow, M. A. Thermal and Light-Induced Spin-Transitions in Iron(II) Complexes of 2,6-Bis(4-halopyrazolyl)pyridines: the Influence of Polymorphism on a Spin-Crossover Compound. *Dalton Trans* **2009**, *2009*, 6656−6666.
(33) Basak, S.; Hui, P.; Chandrasekar, R. Regioselective, One-Pot Syntheses of Symmetrically and Unsymmetrically Halogenated 2',6'-Bispyrazolylpyridines. *Synthesis* **2009**, *2009*, 4042−4048.
(34) Galadzhun, I.; Kulmaczewski, R.; Cespedes, O.; Halcrow, M. A. Iron/2,6-Di(pyrazol-1-yl)pyridine Complexes with a Discotic Pattern of Alkyl or Alkynyl Substituents. *Eur. J. Inorg. Chem.* **2021**, *2021*, 2999−3007.
(35) Craig, G. A.; Costa, J. S.; Teat, S. J.; Roubeau, O.; Yufit, D. S.; Howard, J. A. K.; Aromí, G. Multimetastability in a Spin-Crossover Compound Leading to Different High-Spin-to-Low-Spin Relaxation Dynamics. *Inorg. Chem.* **2013**, *52*, 7203−7209.
(36) Murnaghan, K. D.; Carbonera, C.; Toupet, L.; Griffin, M.; Dîrtu, M. M.; Desplanches, C.; Garcia, Y.; Collet, E.; Létard, J.-F.; Morgan, G. G. Spin-State Ordering on One Sub-lattice of a Mononuclear Iron(III) Spin Crossover Complex Exhibiting LIESST and TIESST. *Chem. − Eur. J.* **2014**, *20*, 5613−5618.
(37) Paradis, N.; Chastanet, G.; Palamarciuc, T.; Rosa, P.; Varret, V.; Boukheddaden, K.; Létard, J.-F. Detailed Investigation of the Interplay Between the Thermal Decay of the Low Temperature Metastable HS State and the Thermal Hysteresis of Spin-Crossover Solids. *J. Phys. Chem. C* **2015**, *119*, 20039−20050.
(38) Gómez, V.; Sáenz de Pipaón, C.; Maldonado-Illescas, P.; Waerenborgh, J. C.; Martin, E.; Benet-Buchholz, J.; Galán-Mascarós, J. R. Easy Excited-State Trapping and Record High T_{TIESST} in a Spin-Crossover Polyanionic Fe^{II} Trimer. *J. Am. Chem. Soc.* **2015**, *137*, 11924−11927.
(39) Weihermüller, J.; Schlamp, S.; Dittrich, B.; Weber, B. Kinetic Trapping Effects in Amphiphilic Iron(II) Spin Crossover Compounds. *Inorg. Chem.* **2019**, *58*, 1278−1289.
(40) Boonprab, T.; Lee, S. J.; Telfer, S. G.; Murray, K. S.; Phonsri, W.; Chastanet, G.; Collet, E.; Trzop, E.; Jameson, G. N. L.; Harding, P.; Harding, D. J. The First Observation of Hidden Hysteresis in an Iron(III) Spin-Crossover Complex. *Angew. Chem. Int. Ed* **2019**, *58*, 11811−11815.
(41) Kiehl, J.; Hochdörffer, T.; Carrella, L. M.; Schünemann, V.; Nygaard, M. H.; Overgaard, J.; Rentschler, E. Pronounced Magnetic Bistability in Highly Cooperative Mononuclear $[Fe(L^{npdtz})_2(NCX)_2]$ Complexes. *Inorg. Chem.* **2022**, *61*, 3141−3151.
(42) Money, V. A.; Carbonera, C.; Elhaïk, J.; Halcrow, M. A.; Howard, J. A. K.; Létard, J.-F. Interplay Between Kinetically Slow

Thermal Spin-Crossover and Metastable High-Spin State Relaxation in an Iron(II) Complex with Similar $T_{1/2}$ and T(LIESST). *Chem. – Eur. J.* **2007**, *13*, 5503–5514.
(43) Hasegawa, Y.; Sakamoto, R.; Takahashi, K.; Nishihara, H. Bis[(*E*)-2,6-bis(1*H*-pyrazol-1-yl)-4-styrylpyridine]iron(II) Complex: Relationship between Thermal Spin Crossover and Crystal Solvent. *Inorg. Chem.* **2013**, *52*, 1658–1665.
(44) Kershaw Cook, L. J.; Thorp-Greenwood, F. L.; Comyn, T. P.; Cespedes, O.; Chastanet, G.; Halcrow, M. A. Unexpected Spin-Crossover and a Low Pressure Phase Change in an Iron(II)/Dipyrazolylpyridine Complex Exhibiting a High-Spin Jahn-Teller Distortion. *Inorg. Chem.* **2015**, *54*, 6319–6330.
(45) Kulmaczewski, R.; Trzop, E.; Kershaw Cook, L. J.; Collet, E.; Chastanet, G.; Halcrow, M. A. Role of Symmetry Breaking in the Structural Trapping of Light-Induced Excited Spin States. *Chem. Commun.* **2017**, *53*, 13268–13271.
(46) Galadzhun, I.; Kulmaczewski, R.; Shahid, N.; Cespedes, O.; Howard, M. J.; Halcrow, M. A. The Flexibility of Long Chain Substituents Influences Spin-Crossover in Isomorphous Lipid Bilayer Crystals. *Chem. Commun.* **2021**, *57*, 4039–4042.
(47) Holland, J. M.; McAllister, J. A.; Kilner, C. A.; Thornton-Pett, M.; Bridgeman, A. J.; Halcrow, M. A. Stereochemical Effects on the Spin-State Transition Shown by Salts of $[FeL_2]^{2+}$ [L = 2,6-Di(pyrazol-1-yl)pyridine]. *J. Chem. Soc., Dalton Trans.* **2002**, *2002*, 548–554.
(48) Money, V. A.; Radosavljevic Evans, I.; Elhaïk, J.; Halcrow, M. A.; Howard, J. A. K. An *X*-ray Powder Diffraction Study of the Spin-Crossover Transition and Structure of Bis(2,6-dipyrazol-1-ylpyrazine)-iron(II) Perchlorate. *Acta Crystallogr. Sect. B: Struct. Sci.* **2004**, *60*, 41–45.
(49) The twinning of phase 2 of $\mathbf{1}[\mathbf{BF_4}]_2$ probably reflects that its unit cell parameters deviate only slightly from their tetragonal values near the phase transition temperature, where the crystals could be grown. Single crystals of $\mathbf{1}[\mathbf{ClO_4}]_2$ were easier to obtain because its unit cell is more strongly monoclinic at room temperature (Table S1).
(50) McCusker, J. K.; Rheingold, A. L.; Hendrickson, D. N. Variable-Temperature Studies of Laser-Initiated $^5T_2 \rightarrow {}^1A_1$ Intersystem Crossing in Spin-Crossover Complexes: Empirical Correlations between Activation Parameters and Ligand Structure in a Series of Polypyridyl Ferrous Complexes. *Inorg. Chem.* **1996**, *35*, 2100–2112.
(51) Brooker, S. Spin Crossover with Thermal Hysteresis: Practicalities and Lessons Learnt. *Chem. Soc. Rev.* **2015**, *44*, 2880–2892.
(52) Pask, C. M.; Greatorex, S.; Kulmaczewski, R.; Baldansuren, A.; McInnes, E. J. L.; Bamiduro, F.; Yamada, M.; Yoshinari, N.; Konno, T.; Halcrow, M. A. Elucidating the Structural Chemistry of a Hysteretic Iron(II) Spin-Crossover Compound from its Copper(II) and Zinc(II) Congeners. *Chem. – Eur. J.* **2020**, *26*, 4833–4841.
(53) Zabala-Lekuona, A.; Seco, J. M.; Colacio, E. Single-Molecule Magnets: From Mn12-ac to Dysprosium Metallocenes, a Travel in Time. *Coord. Chem. Rev.* **2021**, *441*, 213984.
(54) Feng, X.; Mathonière, C.; Jeon, I.-R.; Rouzières, M.; Ozarowski, A.; Aubrey, M. L.; Gonzalez, M. I.; Clérac, R.; Long, J. R. Tristability in a Light-Actuated Single-Molecule Magnet. *J. Am. Chem. Soc.* **2013**, *135*, 15880–15884.
(55) Mathonière, C.; Lin, H.-J.; Siretanu, D.; Clérac, R.; Smith, J. M. Photoinduced Single-Molecule Magnet Properties in a Four-Coordinate Iron(II) Spin Crossover Complex. *J. Am. Chem. Soc.* **2013**, *135*, 19083–19086.
(56) Urtizberea, A.; Roubeau, O. Switchable Slow Relaxation of Magnetization in the Native Low Temperature Phase of a Cooperative Spin-Crossover Compound. *Chem. Sci.* **2017**, *8*, 2290–2295.
(57) Although high-spin $\mathbf{1}[\mathbf{ClO_4}]_2$ is not an SMM, some analogous $[Co(bpp^{R,Y})_2]X_2$ derivatives do have SMM properties.[67−69]
(58) Kershaw Cook, L. J.; Kulmaczewski, R.; Mohammed, R.; Dudley, S.; Barrett, S. A.; Little, M. A.; Deeth, R. J.; Halcrow, M. A. A Unified Treatment of the Relationship Between Ligand Substituents and Spin State in a Family of Iron(II) Complexes. *Angew. Chem. Int. Ed* **2016**, *55*, 4327–4331.
(59) Vela, S.; Novoa, J. J.; Ribas-Arino, J. Insights into the Crystal-Packing Effects on the Spin Crossover of $[Fe^{II}(1\text{-bpp})_2]^{2+}$-Based Materials. *Phys. Chem. Chem. Phys.* **2014**, *16*, 27012–27024.
(60) Mohammed, R.; Chastanet, G.; Tuna, F.; Malkin, T. L.; Barrett, S. A.; Kilner, C. A.; Létard, J.-F.; Halcrow, M. A. The Synthesis of New 2,6-Di(pyrazol-1-yl)pyrazine Derivatives, and the Spin State Behavior of their Iron(II) Complexes. *Eur. J. Inorg. Chem.* **2013**, *2013*, 819–831.
(61) Berdiell, I. C.; Kulmaczewski, R.; Shahid, N.; Cespedes, O.; Halcrow, M. A. The Number and Shape of Lattice Solvent Molecules Controls Spin-Crossover in an Isomorphous Series of Crystalline Solvate Salts. *Chem. Commun.* **2021**, *57*, 6566–6569.
(62) Kulmaczewski, R.; Kershaw Cook, L. J.; Pask, C. M.; Cespedes, O.; Halcrow, M. A. Iron(II) Complexes of 4-(Alkyldisulfanyl)-2,6-di(pyrazolyl)pyridine Derivatives. Correlation of Spin-Crossover Cooperativity with Molecular Structure Following Single-Crystal-to-Single-Crystal Desolvation. *Cryst. Growth Des* **2022**, *22*, 1960–1971.
(63) Suryadevara, N.; Mizuno, A.; Spieker, L.; Salamon, S.; Sleziona, S.; Maas, A.; Pollmann, E.; Heinrich, B.; Schleberger, M.; Wende, H.; Kuppusamy, S. K.; Ruben, M. Structural Insights into Hysteretic Spin-Crossover in a Set of Iron(II)-2,6-Bis(1*H*-pyrazol-1-yl)pyridine) Complexes. *Chem. – Eur. J.* **2022**, *28*, No. e202103853.
(64) Tumanov, S. V.; Veber, S. L.; Greatorex, S.; Halcrow, M. A.; Fedin, M. V. Interplay Between Dopant Species and a Spin-Crossover Host Lattice During Light-Induced Excited-Spin-State Trapping Probed by Electron Paramagnetic Resonance Spectroscopy. *Inorg. Chem.* **2018**, *57*, 8709–8713.
(65) Drahoš, B.; Šalitroš, I.; Císařová, I.; Herchel, R. A Multifunctional Magnetic Material Based on a Solid Solution of Fe(II)/Co(II) Complexes with a Macrocyclic Cyclam-Based Ligand. *Dalton Trans* **2021**, *50*, 11147–11157.
(66) Marchivie, M.; Guionneau, P.; Létard, J.-F.; Chasseau, D. Photo-Induced Spin-Transition: the Role of the Iron(II) Environment Distortion. *Acta Cryst. Sect. B Struct. Sci.* **2005**, *61*, 25–28.
(67) Rigamonti, L.; Bridonneau, N.; Poneti, G.; Tesi, L.; Sorace, L.; Pinkowicz, D.; Jover, J.; Ruiz, E.; Sessoli, R.; Cornia, A. A Pseudo-Octahedral Cobalt(II) Complex with Bispyrazolylpyridine Ligands Acting as a Zero-Field Single-Molecule Magnet with Easy Axis Anisotropy. *Chem. – Eur. J.* **2018**, *24*, 8857–8868.
(68) Garcia-Lopez, V.; Orts-Mula, F.J.; Palacios-Corella, M.; Clemente-Juan, J.M.; Clemente-Leon, M.; Coronado, E. Field-Induced Slow Relaxation of Magnetization in a Mononuclear Co(II) Complex of 2,6-Bis(pyrazol-1-yl)pyridine Functionalized with a Carboxylic Acid. *Polyhedron* **2018**, *150*, 54–60.
(69) Douib, H.; Cornet, L.; Gonzalez, J. F.; Trzop, E.; Dorcet, V.; Gouasmia, A.; Ouahab, L.; Cador, O.; Pointillart, F. Spin-Crossover and Field-Induced Single-Molecule Magnet Behaviour in Metal(II)-Dipyrazolylpyridine Complexes. *Eur. J. Inorg. Chem.* **2018**, *2018*, 4452–4457.

https://doi.org/10.1021/acs.cgd.2c00980
Cryst. Growth Des. 2022, 22, 6809–6817